Supporting Information

When do Anisotropic Magnetic Susceptibilities Lead to Large NMR Shifts? Exploring Particle Shape Effects in the Battery Electrode Material $LiFePO_4$

Roberta Pigliapochi,[†] Liam O'Brien,[‡] Andrew J. Pell,[†,§] Michael W. Gaultois,[†,‖] Yuri Janssen,[¶,⊥] Peter Khalifah,[¶] and Clare P. Grey[*,†]

[†]*Department of Chemistry, University of Cambridge, CB2 1EW Cambridge, UK*

[‡]*Department of Physics, University of Liverpool, L69 7ZE Liverpool, UK*

[¶]*Department of Chemistry, Stony Brook University, NY 11794 Stony Brook, United States*

[§]*Current Address: Department of Materials and Environmental Chemistry, Stockholm University, SE–106 91 Stockholm, Sweden*

[‖]*Current Address: Leverhulme Research Centre for Functional Materials Design, The Materials Innovation Factory, Department of Chemistry, University of Liverpool, Liverpool L7 3NY, UK*

[⊥]*Current Address: Department of Physics, Farmingdale State College, NY 11735 Farmingdale, United States*

E-mail: cpg27@cam.ac.uk

S1. Demagnetising Tensor for Ideal Morphologies

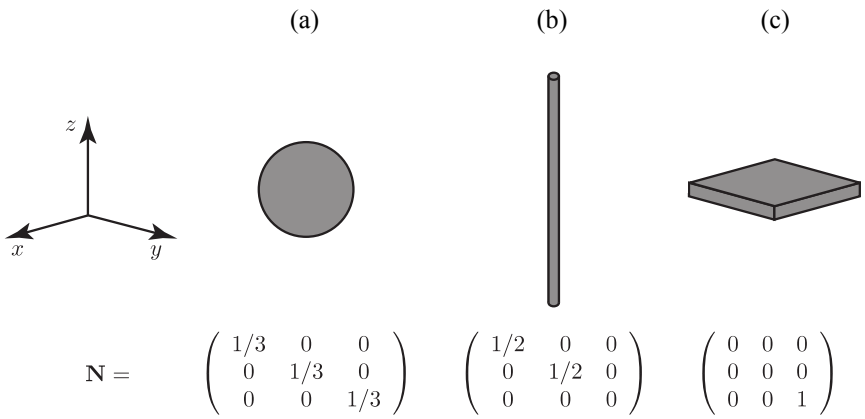

Figure S1: The demagnetising tensors, N, of three uniformly-magnetized crystals. The crystal shapes are (a) a sphere, (b) a cylindrical rod that is infinitely long along the z-direction, and (c) a plane extending to infinity in the x and y dimensions. The axis system is shown to the left. The Figure is reprinted with permission from Ref. 1.

S2. SQUID results of $LiFePO_4$ Single Crystals

Table S1: Results of the linear regression fit of the curves ($\frac{1}{\chi}$ vs T) shown in Figure S2. The R^2 refers to the coefficient of determination in the linear regression.

	Along a	Along b	Along c
Crystal 1	$y = 0.22x + 28.24$, $R^2 = 0.99$	$y = 0.23x + 19.79$, $R^2 = 0.99$	$y = 0.28x + 37.57$, $R^2 = 0.99$
Crystal 2	$y = 0.30x + 32.36$, $R^2 = 0.99$	$y = 0.22x + 16.43$, $R^2 = 0.99$	$y = 0.25x + 23.31$, $R^2 = 0.99$
Crystal 3	$y = 0.23x + 24.90$, $R^2 = 0.99$	$y = 0.21x + 14.63$, $R^2 = 0.99$	$y = 0.30x + 30.68$, $R^2 = 0.99$

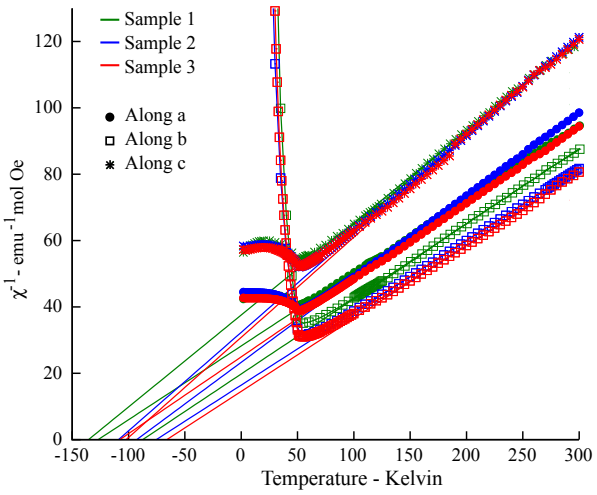

Figure S2: Experimental inverse molar magnetic susceptibility as a function of temperature curves for the three different crystals (green, blue and red for Crystal 1, 2 and 3, respectively).The fitting is shown with the solid lines following the same colouring scheme. The measurement for each crystal mounted with the $a-$, $b-$ or $c-$ axis aligned with the field is represented with circle, square and star symbols, respectively.

S3. TEM and XRD results of $LiFePO_4$ Powder Sample

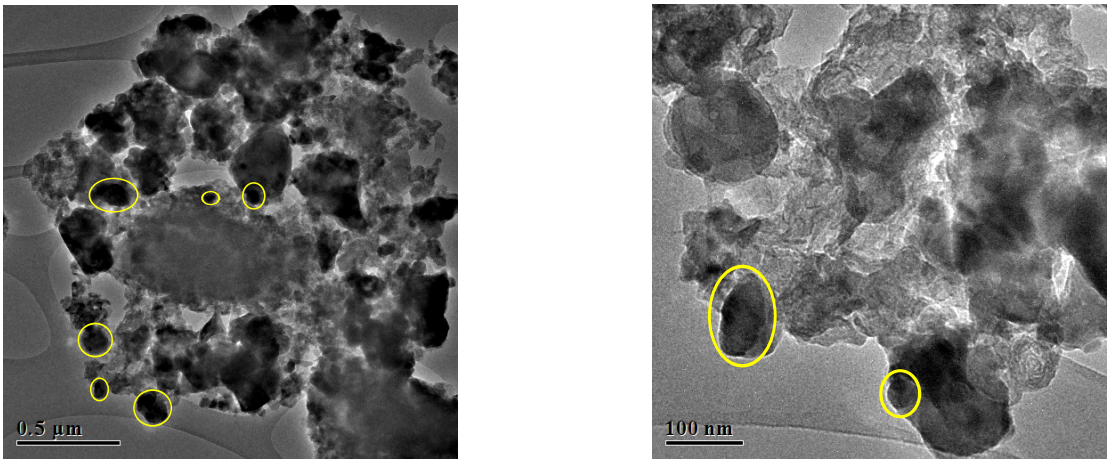

Figure S3: Transmission Electron Microscopy (TEM) images of the $LiFePO_4$ powder sample. The yellow circles highlight $LiFePO_4$ crystallites.

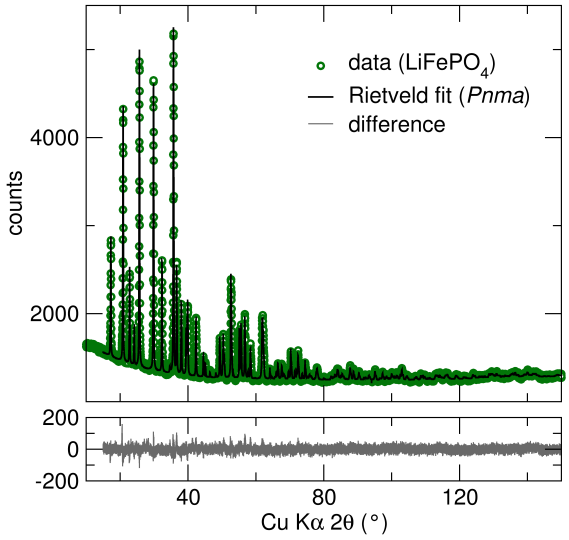

Figure S4: X-ray diffraction pattern for $LiFePO_4$, showing the collected data (green circles), the Rietveld fit (black line) and their difference (lower panel, grey line). The unit cell parameters obtained from the Rietveld refinement are: a-axis 10.3259(1) Å, b-axis 6.00642(7) Å, c-axis 4.69440(6) Å, in agreement with previous results.[2]

S4. MAS NMR results of $LiFePO_4$ Single Crystals

Table S2: Calculated bulk magnetic susceptibility ^{7}Li shift ($\delta^{\mathrm{BMS}}_{\mathrm{calc.}}$) and total isotropic ^{7}Li shift ($\delta^{\mathrm{iso,TOT}}_{\mathrm{calc.}}$) as in eq. 6 of the main article, and experimental isotropic ^{7}Li shift obtained for each crystal aligned along a ($\delta^{\mathrm{iso}}_{\mathrm{exp.}}(a)$), b ($\delta^{\mathrm{iso}}_{\mathrm{exp.}}(b)$), and c ($\delta^{\mathrm{iso}}_{\mathrm{exp.}}(c)$).

	$\delta^{\mathrm{BMS}}_{\mathrm{calc.}}$ ppm	$\delta^{\mathrm{iso,TOT}}_{\mathrm{calc.}}$ ppm	$\delta^{\mathrm{iso}}_{\mathrm{exp.}}(a)$ ppm	$\delta^{\mathrm{iso}}_{\mathrm{exp.}}(b)$ ppm	$\delta^{\mathrm{iso}}_{\mathrm{exp.}}(c)$ ppm
Crystal 1	-5	-21	-19	-22	-23
Crystal 2	-1	-17	-20	-21	-20
Crystal 3	58	42	38	36	38

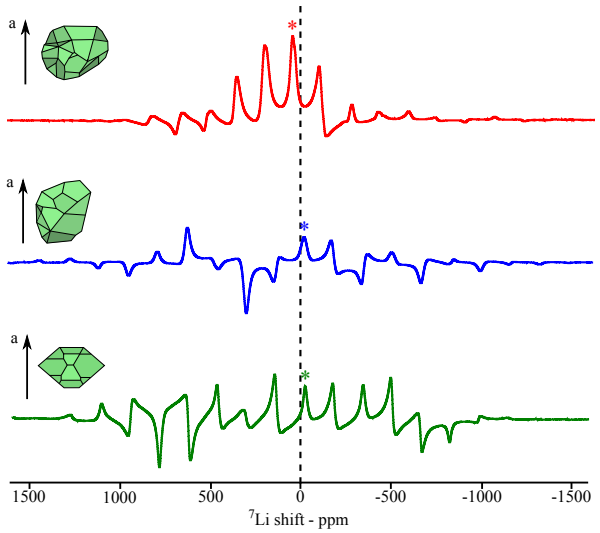

Figure S5: Experimental ^{7}Li NMR spectra of the three $LiFePO_4$ single crystals oriented with the *a*-axis aligned along the magic angle. Green, blue and red lines for Crystal 1, 2 and 3, respectively. The spectra were acquired with the use of the *trigger* function.

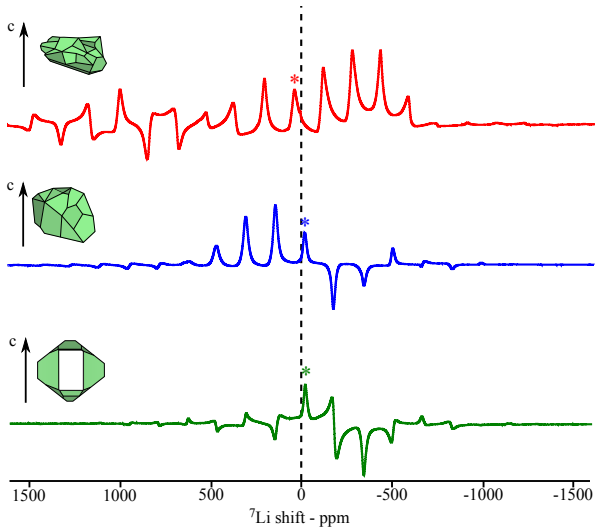

Figure S6: Experimental ^{7}Li NMR spectra of the three $LiFePO_4$ single crystals oriented with the *c*-axis aligned along the magic angle. Green, blue and red lines for Crystal 1, 2 and 3, respectively. The spectra were acquired with the use of the *trigger* function.

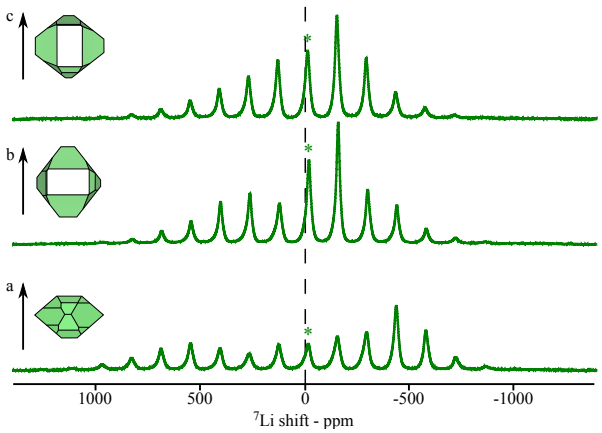

Figure S7: Experimental ^{7}Li NMR spectra of the $LiFePO_4$ single Crystal 1 oriented with the *a*- (bottom), *b*- (middle) and *c*-axis (top) aligned along the magic angle. The spectra were acquired without the use of the *trigger* function.

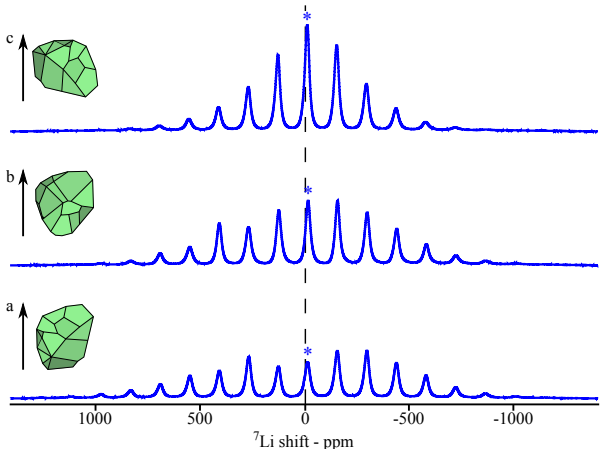

Figure S8: Experimental ^{7}Li NMR spectra of the $LiFePO_4$ single Crystal 2 oriented with the *a*- (bottom), *b*- (middle) and *c*-axis (top) aligned along the magic angle. The spectra were acquired without the use of the *trigger* function.

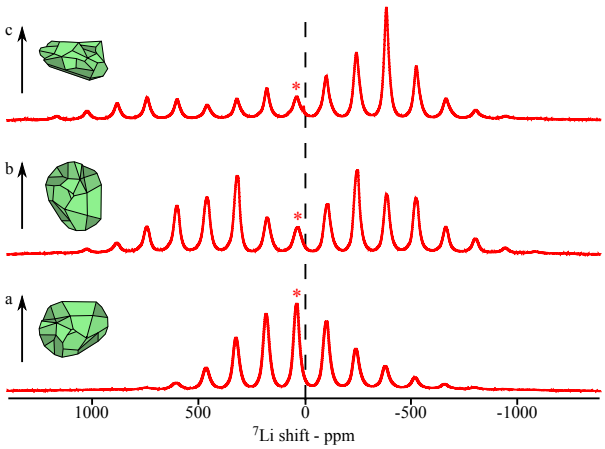

Figure S9: Experimental ^{7}Li NMR spectra of the $LiFePO_4$ single Crystal 3 oriented with the *a*- (bottom), *b*- (middle) and *c*-axis (top) aligned along the magic angle. The spectra were acquired without the use of the *trigger* function.

S5. Static NMR results of $LiFePO_4$ Single Crystals

To characterize the BMS shift anisotropy we measured NMR spectra of the three crystals under static conditions, in which each of the three crystallographic axes was aligned in turn with the external magnetic field. These static ^{7}Li NMR patterns are presented in Figure S10, S11 and S12. Comparing the results obtained for Crystals 1 and 2, we note that the trend of peak positions for the alignment along a, b and c is similar for the two samples (i.e. $\delta_a > \delta_c > \delta_b$). However, for Crystal 3 the relative positions of δ_b and δ_c do not follow the same trend (i.e. $\delta_a > \delta_b \approx \delta_c$). In order to understand these trends, we calculated the static ^{7}Li NMR spectra.

The shift tensor can be expressed as $\boldsymbol{\delta}^{\mathrm{TOT}}_{\mathrm{calc.}} = \boldsymbol{\delta}^{\mathrm{BMS}}_{\mathrm{calc.}} + \boldsymbol{\delta}^{\mathrm{dip}}_{\mathrm{calc.}} + \delta^{s}_{\mathrm{local}} \cdot \mathbf{1}$. The resulting rank-zero terms contribute tothe isotropic shift, the rank-two terms contribute to the shift anisotropy, and the rank-one terms do not give rise to observable features under high-field conditions.[1,3] Here, the $\boldsymbol{\delta}^{\mathrm{BMS}}_{\mathrm{calc.}}$ term corresponds to the BMS tensor calculated as described in the Experimental Section of the main article. As a reminder, this tensor is dependent on the morphology and the magnetic susceptibility of each sample, and it is hence calculated specifically for each single crystal. The term $\boldsymbol{\delta}^{\mathrm{dip}}_{\mathrm{calc.}}$ corresponds to the spin-dipolar hyperfine interaction of the Li site with the neighbouring Fe centres within the Ewald sphere. Some of the present authors have previously calculated this contribution for $LiFePO_4$ in Ref. 4. The results of $\boldsymbol{\delta}^{\mathrm{dip}}_{\mathrm{calc.}}$ are summarised in the next Section. Finally, the $\delta^{s}_{\mathrm{local}} \cdot \mathbf{1}$ term corresponds to the diagonal tensor which has the local isotropic shift contribution as each diagonal element (in this work: $\delta^{s}_{\mathrm{local}} = -16$ ppm, as in Figure 4 of the main article). We note that this simplified formalism neglects the contributions arising from the zero-field splitting term, as well as the effects due to the coupling between the Fermi contact hyperfine term and the anisotropic component of the g-shift tensor. Both these contributions have been shown to be very small for the ^{7}Li shift tensor in $LiFePO_4$. A more comprehensive description of the full tensor can be found in the works of Pigliapochi *et al.*[4] and Mondal *et al.*[5]

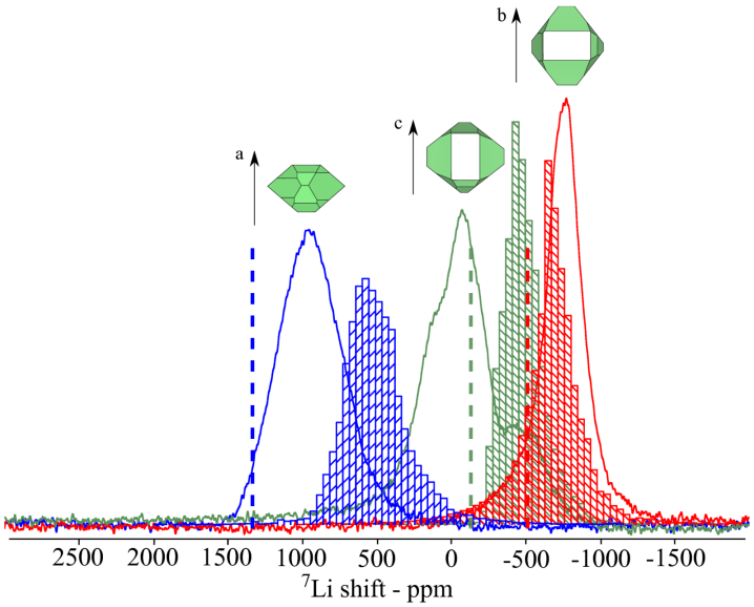

Figure S10: Comparison of the experimental static ^{7}Li solid-state NMR spectra obtained for Crystal 1 at three orientations, with the corresponding calculated spectra. The experimental static ^{7}Li NMR spectra oriented with the *a*- (red), *b*- (blue) and *c*-axis (green) aligned along the rotor axis (magic angle) are shown with solid lines. The simulation of the static pattern for the three orientations is presented with the histograms, following the same colouring scheme. The dotted lines indicate the values of $\boldsymbol{\delta}^{\text{dip}}_{\text{calc.}} + \delta^{s}_{\text{local}} \cdot \mathbf{1}$ for $B_0 \parallel a$ (blue dotted line), $B_0 \parallel b$ (red dotted line) and $B_0 \parallel c$ (green dotted line).

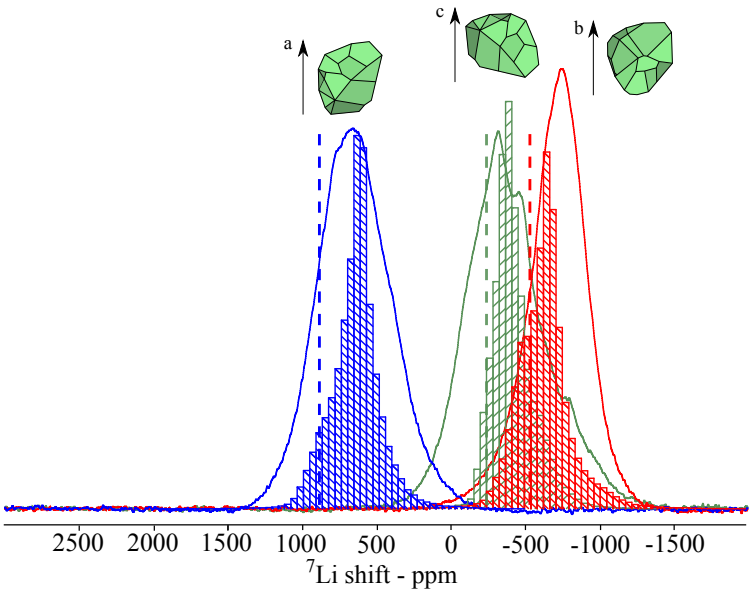

Figure S11: Comparison of the experimental static ^{7}Li solid-state NMR spectra obtained for Crystal 2 at three orientations, with the corresponding calculated spectra. The experimental static ^{7}Li NMR spectra oriented with the *a*- (red), *b*- (blue) and *c*-axis (green) aligned along the rotor axis (magic angle) are shown with solid lines. The simulation of the static pattern for the three orientations is presented with the histograms, following the same colouring scheme. The dotted lines indicate the values of $\boldsymbol{\delta}^{\text{dip}}_{\text{calc.}} + \delta^{s}_{\text{local}} \cdot \mathbf{1}$ for $B_0 \parallel a$ (blue dotted line), $B_0 \parallel b$ (red dotted line) and $B_0 \parallel c$ (green dotted line).

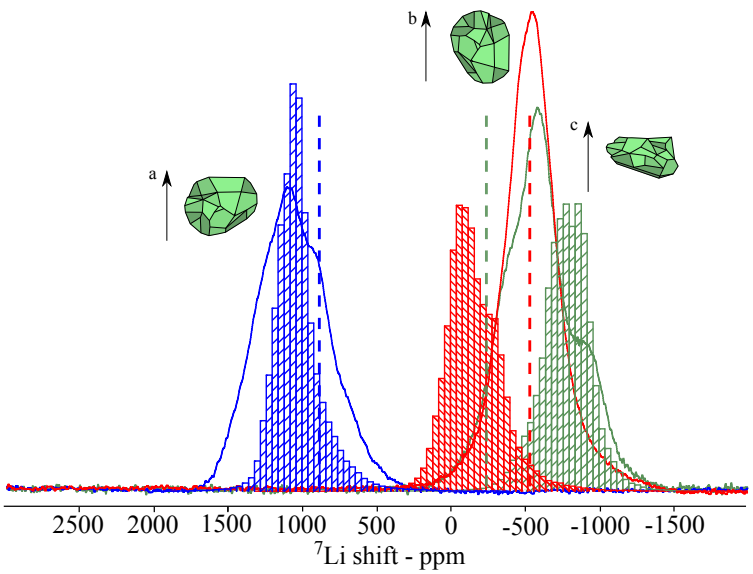

Figure S12: Comparison of the experimental static ^{7}Li solid-state NMR spectra obtained for Crystal 3 at three orientations, with the corresponding calculated spectra. The experimental static ^{7}Li NMR spectra oriented with the a- (red), b- (blue) and c-axis (green) aligned along the rotor axis (magic angle) are shown with solid lines. The simulation of the static pattern for the three orientations is presented with the histograms, following the same colouring scheme. The dotted lines indicate the values of $\boldsymbol{\delta}^{\mathrm{dip}}_{\mathrm{calc.}} + \delta^{s}_{\mathrm{local}} \cdot \mathbf{1}$ for $B_0 \parallel a$ (blue dotted line), $B_0 \parallel b$ (red dotted line) and $B_0 \parallel c$ (green dotted line).

The contribution to the ^{7}Li shift anisotropy resulting from the local interactions ($\boldsymbol{\delta}^{\mathrm{dip}}_{\mathrm{calc.}} + \delta^{s} \cdot \mathbf{1}$) is independent of the sample morphology. Hence, the corresponding values for $B_0 \parallel a$, $B_0 \parallel b$ and $B_0 \parallel c$ are equal for every Crystal, and are indicated with the dotted lines in Figures S10 to S12. The experimental ^{7}Li NMR spectra of the three crystals, however, show that the shifts vary between the different crystals. The effect of the sample shape on the shift anisotropy is introduced by including the $\boldsymbol{\delta}^{\mathrm{BMS}}_{\mathrm{calc.}}$ contribution calculated for each crystal. The results of the calculations corresponding to $\boldsymbol{\delta}^{\mathrm{TOT}}_{\mathrm{calc.}}$ are shown as histograms in Figures S10 to S12. As pointed out earlier, the modelled crystal shapes are approximate, and this approximation is believed to be the major source of discrepancy between the experimental and the calculated ^{7}Li NMR spectra. Nevertheless, the comparison shows that our approach to the calculation of the BMS effects is able to broadly reproduce the distribution of demagnetising fields across each crystal, and the resulting distribution of BMS shifts. These are found to contribute significantly to the ^{7}Li shift and shift anisotropy for the different

sample morphologies. In particular, we highlight that the trend of increasing total shift for $B_0 \parallel c$ between Crystal 1, 2 and 3 qualitatively agrees well with the experimental data. This agreement is critical, as it reflects the most prominent change in shape between crystals (i.e. the reduction in c-axis dimension, relative to a and b), hence the dominant effect of the BMS shift.

S6. A^{dip} calculation – DFT results

The following results refer to the work of Pigliapochi *et al.*,[4] and are only summarised here for convenience. They were obtained for $LiFePO_4$ using the CRYSTAL code[6] and the hybrid PBE0 functional.[7] Full details can be found in Ref. 4.

The four Li sites Li1 to Li4 of the $LiFePO_4$ in Figure S13 occupy the same 1a Wyckoff position, and are related by symmetry (axial glide reflection or twofold screw rotation), as defined by the orthorombic *Pnma* space group.

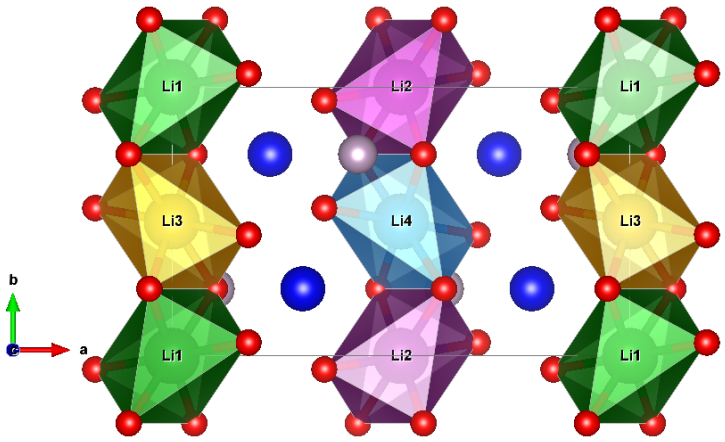

Figure S13: Repeating unit of the olivine-type phase of $LiFePO_4$. The four octahedral Li sites are labelled 1, 2, 3, 4 and occupy different spatial positions: their environments (in green, purple, yellow and blue respectively) are related to one another according to the orthorhombic symmetry of the *Pnma* space group.

If expressed with respect to its principle axis frame, each Li position in Figure S13 has the same dipolar hyperfine shift tensor, $\boldsymbol{\delta}^{\mathrm{dip}}$. However, if all Li1($\boldsymbol{\delta}^{\mathrm{dip}}$), Li2($\boldsymbol{\delta}^{\mathrm{dip}}$), Li3($\boldsymbol{\delta}^{\mathrm{dip}}$)

and Li4($\boldsymbol{\delta}^{\mathrm{dip}}$) are expressed with respect to the $LiFePO_4$ unit cell, then these tensors are rotated with respect to one another as dictated by the symmetry operations of the *Pnma* space group.[4]

From the results of the DFT calculation obtained in Ref. 4, the Li1($\boldsymbol{\delta}^{\mathrm{dip}}$), Li2($\boldsymbol{\delta}^{\mathrm{dip}}$), Li3($\boldsymbol{\delta}^{\mathrm{dip}}$) and Li4($\boldsymbol{\delta}^{\mathrm{dip}}$) with respect to the a, b, c $LiFePO_4$ unit cell frame are:

$$\mathrm{Li1} : \boldsymbol{\delta}^{\mathrm{dip}} = \begin{pmatrix} 866.00 & 126.47 & 80.42 \\ 126.47 & -513.61 & -39.46 \\ 80.42 & -39.46 & -352.39 \end{pmatrix} \text{ ppm}$$

$$\mathrm{Li2} : \boldsymbol{\delta}^{\mathrm{dip}} = \begin{pmatrix} 866.06 & 126.47 & -80.31 \\ 126.47 & -513.61 & 39.31 \\ -80.31 & 39.31 & -352.41 \end{pmatrix} \text{ ppm}$$

$$\mathrm{Li3} : \boldsymbol{\delta}^{\mathrm{dip}} = \begin{pmatrix} 866.10 & -126.51 & 80.47 \\ -126.51 & -513.64 & 39.49 \\ 80.47 & 39.49 & -352.46 \end{pmatrix} \text{ ppm}$$

$$\mathrm{Li4} : \boldsymbol{\delta}^{\mathrm{dip}} = \begin{pmatrix} 866.12 & -126.49 & -80.23 \\ -126.49 & -513.69 & -39.28 \\ -80.23 & -39.28 & -352.43 \end{pmatrix} \text{ ppm}$$

If we include the isotropic shift ($\delta^s = -16$ ppm) to the diagonal components, we get:

$$\text{Li1} : \delta^s \cdot \mathbf{1} \; + \; \boldsymbol{\delta}^{\text{dip}} = \begin{pmatrix} 850.00 & 126.47 & 80.42 \\ 126.47 & -529.61 & -39.46 \\ 80.42 & -39.46 & -368.39 \end{pmatrix} \text{ppm}$$

$$\text{Li2} : \delta^s \cdot \mathbf{1} \; + \; \boldsymbol{\delta}^{\text{dip}} = \begin{pmatrix} 850.06 & 126.47 & -80.31 \\ 126.47 & -529.61 & 39.31 \\ -80.31 & 39.31 & -368.41 \end{pmatrix} \text{ppm}$$

$$\text{Li3} : \delta^s \cdot \mathbf{1} \; + \; \boldsymbol{\delta}^{\text{dip}} = \begin{pmatrix} 850.10 & -126.51 & 80.47 \\ -126.51 & -529.64 & 39.49 \\ 80.47 & 39.49 & -368.46 \end{pmatrix} \text{ppm}$$

$$\text{Li4} : \delta^s \cdot \mathbf{1} \; + \; \boldsymbol{\delta}^{\text{dip}} = \begin{pmatrix} 850.12 & -126.49 & -80.23 \\ -126.49 & -529.69 & -39.28 \\ -80.23 & -39.28 & -368.43 \end{pmatrix} \text{ppm}$$

S7. Crystal mask and BMS shift calculation details

Table S3: Plane indices h, k, l, and distance from chosen crystal origin, d, for the identified facets of Crystal 1. Basis follows the crystal unit cell: a, b, c. The volume enclosed by these planes forms the modelled crystal in micromagnetic simulations. Note, the demagnetising field is scale invariant (on lengthscales over which the continuum approximation is valid), and only relative values of d are necessary to define the crystal shape. As such quoted d values are in arbitrary units.

h	k	l	d (arb.)
1	0	-1	48.8
-1	0	1	-12.6
1	0	1	-15.1
-1	0	-1	50.1
1	1	1	7.5
-1	-1	-1	28.8
1	0	0	9.8
-1	0	0	16.4
1	1	-1	58.8
-1	-1	1	-21.7
0	-1	1	-26.6
0	1	-1	60.5
1	-1	1	-23.4
-1	1	-1	60.2
1	-1	-1	26.8
-1	1	1	9.2
0	-1	-1	27.6
0	1	1	6.6
-2	0	1	-5.6
2	0	-1	41.6
-2	0	-1	44.6
2	0	1	-9.2
2	-1	0	-5.4
-2	1	0	33.6
-2	-1	0	-2.4
2	1	0	30.6

To calculate the isotropic BMS shift under MAS, it is sufficient to take the average value of on-diagonal components of $\boldsymbol{N}(\boldsymbol{r})$ when calculating equation 5 of the main article, since any dispersion in the values produces only line broadening in this case. The resulting average demagnetising tensor, $\boldsymbol{N}^{\mathbf{iso}}$, for the three crystals under investigation are shown below, while $\delta^{\mathrm{BMS}}_{\mathrm{calc.}}$ are shown in table 2 of the main article.

$$\text{Crystal1} : N^{\text{iso}} = \begin{pmatrix} 0.41 & 0 & 0 \\ 0 & 0.30 & 0 \\ 0 & 0 & 0.29 \end{pmatrix}$$

$$\text{Crystal2} : N^{\text{iso}} = \begin{pmatrix} 0.38 & 0 & 0 \\ 0 & 0.32 & 0 \\ 0 & 0 & 0.30 \end{pmatrix}$$

$$\text{Crystal3} : N^{\text{iso}} = \begin{pmatrix} 0.27 & 0 & 0 \\ 0 & 0.21 & 0 \\ 0 & 0 & 0.51 \end{pmatrix}$$

S8. Ternary plot of the BMS shift variation as a function of the demagnetising shift tensor

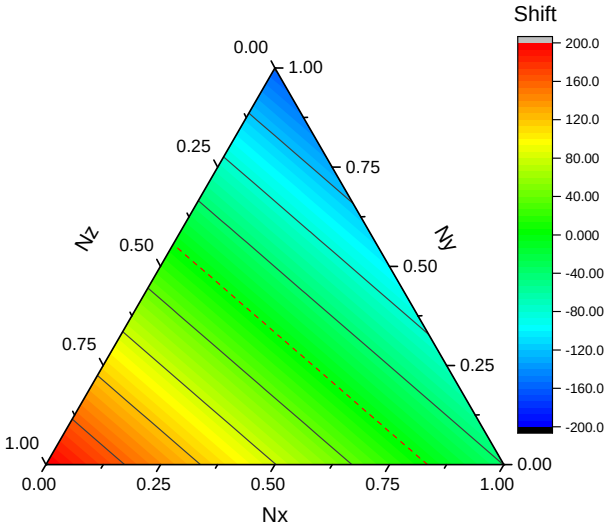

Figure S14: Analysis of the calculated BMS shift for $LiFePO_4$ powder crystallites. The variation of the BMS shift is shown as a function of the principal components of the demagnetising tensor, N_x (a-axis), N_y (b-axis) N_z (c-axis). The colouring in the plot represents the δ(BMS) as determined by the relative (N_a vs N_b) morphology of the $LiFePO_4$ particle. The colouring scheme, indicated on the right-hand side, corresponds to the δ(BMS) range from -150 ppm (dark blue) to $+200$ ppm (red). The solid lines represent $+25$ ppm increments, and the dotted red line indicates 0 ppm.

References

(1) Pell, A. J.; Pintacuda, G.; Grey, C. P. *Paramagnetic NMR in solution and the solid state*; Elsevier, 2018.

(2) Streltsov, V. A.; Belokoneva, E.; Tsirelson, V.; Hansen, N. Multipole analysis of the electron density in triphylite, $LiFePO_4$, using X-ray diffraction data. *Acta Crystallographica Section B* **1993**, *49*, 147–153.

(3) Pennanen, T. O.; Vaara, J. Nuclear magnetic resonance chemical shift in an arbitrary electronic spin state. *Physical review letters* **2008**, *100*, 133002.

(4) Pigliapochi, R.; Pell, A. J.; Seymour, I. D.; Ceresoli, D.; Kaupp, M.; Grey, C. P. DFT investigation of the effect of spin-orbit coupling on the NMR shifts in paramagnetic solids. *Physical Review B* **2017**, *95*, 054412.

(5) Mondal, A.; Kaupp, M. Quantum-Chemical Approach to NMR Chemical Shifts in Paramagnetic Solids Applied to $LiFePO_4$ and $LiCoPO_4$. *The Journal of Physical Chemistry Letters* **2018**, *9*, 1480–1484.

(6) Dovesi, R.; Orlando, R.; Civalleri, B.; Roetti, C.; Saunders, V. R.; Zicovich-Wilson, C. M. CRYSTAL: a computational tool for the ab initio study of the electronic properties of crystals. *Zeitschrift für Kristallographie* **2005**, *220*, 571–573.

(7) Perdew, J. P.; Burke, K.; Ernzerhof, M. Generalized gradient approximation made simple. *Physical review letters* **1996**, *77*, 3865.